Resolution Enhancement in High Resolution Wide Swath MIMO SAR

Ultra High Resolution Wide Swath MIMO SAR

Mohammed AlShaya
IDCOM, University of Edinburgh, UK
KACST, KSA
mohammed.alshaya@ed.ac.uk

Mehrdad Yaghoobi
IDCOM, University of Edinburgh, UK
m.yaghoobi-vaighan@ed.ac.uk

Bernard Mulgrew
IDCOM, University of Edinburgh, UK
bernie.mulgrew@ed.ac.uk

***Abstract*—A new multiple-input multiple-output (MIMO) SAR configuration using multiple adjacent azimuth beams are proposed to map wider image swaths with higher cross-range resolution in comparison with the conventional MIMO SAR. The proposed configuration allows to utilise all the phase centres including the overlapping ones to reduce the minimum operating pulse repetition frequency (PRF) unlike the case of the conventional MIMO SAR in which only the non-overlapped phase centres and one of each overlapped phase centres are utilised. The waveforms used for transmission share the same bandwidth and have the same centre frequency. Each transmitted waveform consists of a sequence of sub-pulses consisting of conventional linear frequency modulated (LFM) waveforms and the echoes corresponding to different phase centres are separated at the receiver using digital beamforming (DBF) on receive in elevation. The estimated range profile has the property of inter-range cell interference (IRCI) free as a frequency domain system identification (FDSI)-based estimation algorithm is used to identify the impulse response in the range dimension. Finally, simulated data is used to validate the effectiveness of the proposed configuration.**

***Index Terms*—MIMO, system identification, LFM, SAR, Radar**

I. Introduction

The concept of MIMO SAR has been first introduced in [1] where the possibility of obtaining a high resolution wide swath image is explained. It is due to the extra phase centres introduced by the use of multiple transmitters along with multiple receiving channels. The most challenging issue in MIMO SAR is to design multiple orthogonal waveforms in a way that the orthogonality holds regardless of the time delays and Doppler shifts [2].

Different waveforms are proposed in the literature for MIMO SAR such as the one in [3] [4] in which up and down-chirps are used to generate a sophisticated waveform. The author in [2] proposed short-term shift orthogonal waveforms which uses digital beamforming on receive in elevation to suppress distant scatterers. A class of LFM based MIMO waveforms along with digital beamforming (DBF) in elevation is proposed in [5] to solve the orthogonality problem of MIMO SAR waveforms. According to the literature, the minimum PRF in MIMO SAR should satisfy the inequality $\mathrm{PRF}_{min} \geq B_d/K_p$ where B_d denotes the Doppler bandwidth and K_p is the number of non-overlapping phase centres which is equal to $M + N - 1$ for the case when the number of transmitters (M) is the same as the number of receivers (N) and the same antenna arrays are used for both transmission and reception. In [6] we proposed multiple sub-band MIMO SAR with multiple azimuth beams in order to utilise the available bandwidth to the maximum efficiency.

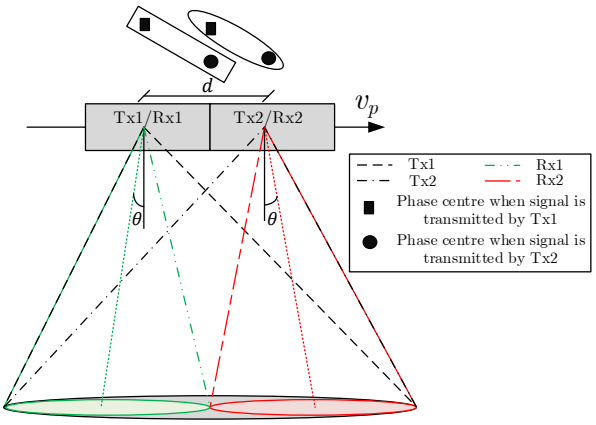

Fig. 1. The proposed MIMO SAR configuration where the phase centres surrounded by a rectangular indicate that the signals are received by the first receiver and occupy the the first half of the Doppler bandwidth and the phase centres surrounded by an ellipse indicate that the signals are received by the second receiver and occupy the second half of the Doppler bandwidth. The wide transmit beams are synthesised from the narrow beams as described in Fig.2. Each receiver consists of N_{el} elevation channels. v_p is the platform velocity

In this paper, we propose a new MIMO SAR configuration shown in Fig.1 in which multiple adjacent receiving sub-beams with different phase centres and squint angles are generated in th azimuth direction and the wide beams of the transmitters are synthesised from the narrow beams as shown in Fig.2. The waveform used for transmission is a sequence of sub-pulses consisting of conventional LFM waveforms and the echoes corresponding to different phase centres are separated at the receiver using digital beamforming (DBF) on receiving in elevation and null-steering technique. This is possible because echoes corresponding to different sub-pulses (i.e. phase centres) arrive at each instant of time from different elevation angles. In addition, a frequency domain system identification (FDSI)-based estimation algorithm [6] is used to identify the impulse response in the range dimension which has the property of inter-range cell interference (IRCI) free which is ideally having a zero side-lobe level in the estimated range profile. The main advantage of the proposed configuration

is that all of the phase centres are utilised (i.e. even the overlapping ones) and thus, the minimum PRF should satisfy the inequality $\mathrm{PRF}_{min} \geq B_d/(MN)$ which provides the opportunity to map wider image swaths with higher cross-range resolution in comparison with the conventional MIMO SAR.

Notations. Matrices are denoted by upper case bold letters (e.g. $\mathbf{A}$) while scalars and vectors are denoted by upper\lower case letters (e.g. a and A) and bold lower case letters (e.g. $\mathbf{a}$), respectively. In addition, $(.)^T$ and $(.)^H$ denote the transpose operator and hermitian operator, respectively. $\mathrm{diag}(\mathbf{a})$ denotes a matrix with vector $\mathbf{a}$ as main diagonal. $\mathcal{C}$ represents the field of complex numbers.

II. MIMO SAR System Model

Consider a narrowband MIMO radar system with an array of M antenna elements at the transmitter and an array of N antenna elements at the receiver. The baseband received signal at i^{th} elevation channel in the n^{th} receiving azimuth aperture and can be expressed as

$$y_{n,i}(t,\eta) = \sum_{m=1}^{M}\sum_{l=0}^{L-1}\sigma_l e^{-j2\pi F_c \tau_{l,mn}(\eta)} a_i(\phi_l))x(t-\tau_{l,mn}(\eta) - \mid n-m \mid t_d) + w_n(t) \quad (1)$$

where,

$$a_i(\phi_l) = e^{j2\pi i d_{\mathrm{el}} \sin(\phi_l)/\lambda}, \quad i = 0,1,...,N_{\mathrm{el}}-1 \quad (2)$$

$x(t)$ is a known waveform (i.e. LFM waveform), t and η denote the fast time and slow time, respectively. F_c denotes the carrier frequency, σ_l is the radar cross-section (RCS) of the scattering point located at the l^{th} range cell of the swath, $\tau_{l,mn}(\eta)$ is the round trip delay of the l^{th} scattering point when the waveform is transmitted by the m^{th} transmitter and received by the n^{th} receiver, t_d denotes a delay between the transmitted sub-pulses which includes the beam switching time (t_{sw}), d_{el} denotes the distance between the elevation channels, N_{el} is the number of elevation channels, ϕ_l is the elevation angle of the l^{th} range cell, λ denotes the wavelength and $w_n(t)$ is additive white noise generated by the n^{th} receiver.

Without loss of generality, consider the case when $M = N = 2$ as shown in Fig.1. The timing diagram of the transmitting waveforms is as shown in Fig.2 . The received

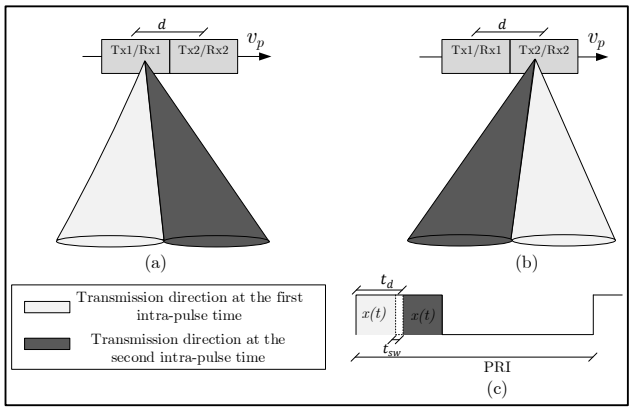

Fig. 2. Generation of synthesised wide transmission beams from narrow beams. (a) Transmission directions sequence of the first transmitter. (b) Transmission directions sequence of the second transmitter. (c) Timing structure of a single PRI transmitted by the m^{th} transmitter where t_{sw} denotes the beam switching time.

signals at the receivers can be expressed as the following,

$$y_{1,i}(t,\eta) = \sum_{l=0}^{L-1}\sigma_l e^{-j2\pi F_c \tau_{l,11}(\eta)} a_i(\phi_l))x(t-\tau_{l,11}(\eta)) + \sum_{l=0}^{L-1}\sigma_l e^{-j2\pi F_c \tau_{l,21}(\eta)} a_i(\phi_l))x(t-\tau_{l,21}(\eta)-t_d) + w_1(t) \quad (3)$$

$$y_{2,i}(t,\eta) = \sum_{l=0}^{L-1}\sigma_l e^{-j2\pi F_c \tau_{l,12}(\eta)} a_i(\phi_l))x(t-\tau_{l,12}(\eta)-t_d) + \sum_{l=0}^{L-1}\sigma_l e^{-j2\pi F_c \tau_{l,22}(\eta)} a_i(\phi_l))x(t-\tau_{l,22}(\eta)) + w_2(t) \quad (4)$$

where $\tau_{l,11}(\eta) = \frac{2R_{l,1}(\eta)}{c}$, $\tau_{l,22}(\eta) = \frac{2R_{l,2}(\eta)}{c}$ and $\tau_{l,12}(\eta) = \tau_{l,21}(\eta) = \frac{R_{l,1}(\eta)+R_{l,2}(\eta)}{c}$. $R_{l,1}$ and $R_{l,2}$ are the slant range from the first transmitter to the l^{th} scattering point and from the second transmitter to the l^{th} scattering point, respectively, and can be expressed under the assumption of a straight sensor trajectory and approximated using Taylor expansion to the second order as the following [6],

$$R_{l,1}(\eta) \approx R_l - v_p \sin(\theta_1)(\eta + \frac{d}{2v_p}) + \frac{v_p^2 \cos^2(\theta_1)(\eta + d/(2v_p))^2}{2R_l} \quad (5)$$

$$R_{l,2}(\eta) \approx R_l - v_p \sin(\theta_2)(\eta - \frac{d}{2v_p}) + \frac{v_p^2 \cos^2(\theta_2)(\eta - d/(2v_p))^2}{2R_l} \quad (6)$$

where θ_n denotes the squint angle of the n^{th} receiving beam, R_l is the slant range to the l^{th} scatterer when $\eta = 0$. Quadratic approximation of $R_{l,1}(\eta) + R_{l,2}(\eta)$ can be expressed as the following,

$$R_{l,1}(\eta) + R_{l,2}(\eta) \approx 2R_{l,1}(\eta - \frac{d}{2v_p})_{\theta=\theta_{Rx}} + \frac{d^2}{4R_l} \quad (7)$$

where θ_{Rx} denotes the squint angle of the receiver. The received signals in (3) and (4) are sampled from the range cell that corresponds to the near range to the range cell that corresponds to the far range with a sampling frequency of $f_s = 1/T_s$. The signals are also sampled in the azimuth dimension with a sampling frequency of $f_p = \text{PRF}$ which is the pulse repetition frequency. The discrete time version of the received signal can be expressed as the following,

$$z_{1,i}[n_t, n_a] = \sum_{l=0}^{L-1} \underbrace{(h_{11,i}[l, n_a] + h_{21,i,d}[l, n_a])}_{h_{1,i}[l,n_a]} x[n_t - l] + w_1[n_t] \quad (8)$$

$$z_{2,i}[n_t, n_a] = \sum_{l=0}^{L-1} \underbrace{(h_{12,i,d}[l, n_a] + h_{22,i}[l, n_a])}_{h_{2,i}[l,n_a]} x[n_t - l] + w_2[n_t] \quad (9)$$

where,

$$h_{mn,i}[l, n_a] = \underbrace{\sigma_l e^{-j2\pi F_c \tau_{l,mn}(n_a)}}_{h_{mn}[l,n_a]} a_i(\phi_l), \quad (10)$$

$$h_{mn,i,d}[l, n_a] = h_{mn,i}[l - l_d, n_a], \quad (11)$$

$l_d = t_d/T_s$, n_t and n_a are the range and azimuth time indices, respectively.

III. Azimuth Ambiguity Removal and Image Formation

The effective sampling frequency in the azimuth dimension is $\text{PRF} = B_d/(MN)$ where B_d is the Doppler bandwidth so it is expected to have an azimuth ambiguity. It should be noted that the Doppler bandwidth of each of the received signals expressed in (8) and (9) is B_d/N which corresponds to the receiving beamwidth.

The aliased Doppler spectrum of the signal received at a given receiver can be perfectly reconstructed if there are M independent representations of the aliased signal in accordance to the multi-aperture reconstruction algorithm [1]. In our case, the $M = 2$ independent representations of the impulse response measured from the first receiver are $h_{11,i}$ and $h_{21,i}$ which can be used to reconstruct the aliased Doppler spectrum that corresponds to the first receiving beamwidth. Similarly, the $M = 2$ independent representations of the impulse response measured from the second receiver are $h_{12,i}$ and $h_{22,i}$ which can be used to reconstruct the aliased Doppler spectrum that corresponds to the second receiving beamwidth. The location of the phase centres that corresponds to different Doppler bandwidth is illustrated in Fig.1.

The separation of the impulse responses that correspond to different phase centres can be done by digital beamforming (DBF) in elevation on receive by exploiting the relation between time delay and elevation angle in a side-looking radar imaging geometry. This relation results in that echoes corresponding to different transmitted sub-pulses (i.e. phase centres) arrive at each instant of time from different elevation angles. Finally, the reconstructed Doppler bandwidth of the receivers should be combined to form the full Doppler bandwidth B_d as explained next.

A. Impulse Response Estimation and DBF in Elevation

The impulse responses $h_{1,i}$ and $h_{2,i}$ in (8) and (9) will be estimated individually using the FDSI-based estimation algorithm proposed in [6]. It should be noted that each of the impulse responses $h_{1,i}$ and $h_{2,i}$ occupies half the Doppler bandwidth. Accordingly, the Doppler bandwidths need to be combined after removing the azimuth ambiguity to form the full Doppler bandwidth.

The received signals in (8) and (9) can be written in a matrix form for a given azimuth bin as

$$\mathbf{z}_{1,i}[n_a] = \left[z_{1,i}[0, n_a], z_{1,i}[1, n_a], ..., z_{1,i}[K + L - 1, n_a]\right]^T = \mathbf{X}\mathbf{h}_{1,i}[n_a] + \mathbf{w}_1[n_a] \quad (12)$$

$$\mathbf{z}_{2,i}[n_a] = \left[z_{2,i}[0, n_a], z_{2,i}[1, n_a], ..., z_{2,i}[K + L - 1, n_a]\right]^T = \mathbf{X}\mathbf{h}_{2,i}[n_a] + \mathbf{w}_2[n_a] \quad (13)$$

where K is the length of the waveform transmitted. The matrix $\mathbf{X}$ can be made circulant and accordingly, the channel impulse responses $\mathbf{h}_{1,i}[n_a]$ and $\mathbf{h}_{2,i}[n_a]$ are zero padded by $(K-1)$ as the following,

$$\mathbf{z}_{1,i}[n_a] = \mathbf{X}_C[n_a] \underbrace{\begin{bmatrix}\mathbf{h}_{1,i}[n_a] \\ \mathbf{0}_{(K-1)}\end{bmatrix}}_{\mathbf{h}_{1,i,p}[n_a]} + \mathbf{w}_1[n_a] \quad (14)$$

$$\mathbf{z}_{2,i}[n_a] = \mathbf{X}_C[n_a] \underbrace{\begin{bmatrix}\mathbf{h}_{2,i}[n_a] \\ \mathbf{0}_{(K-1)}\end{bmatrix}}_{\mathbf{h}_{2,i,p}[n_a]} + \mathbf{w}_2[n_a] \quad (15)$$

The channel impulse responses can be estimated as the following,

$$\hat{\mathbf{h}}_{1,i,p}[n_a] = \mathbf{X}_C^{-1}[n_a]\mathbf{z}_{1,i}[n_a] \quad (16)$$

$$\hat{\mathbf{h}}_{2,i,p}[n_a] = \mathbf{X}_C^{-1}[n_a]\mathbf{z}_{2,i}[n_a] \quad (17)$$

The estimation in (16) and (17) can be performed easily in the frequency domain by exploiting the DFT structure of $\mathbf{X}_C[n_a]$ after being decomposed as the following,

$$\mathbf{X}_C[n_a] = \mathbf{F}\text{diag}\{\mathcal{X}\}\mathbf{F}^H \quad (18)$$

where $\mathcal{X}$ is the Fourier transform of the first row of the matrix $\mathbf{X}_C[n_a]$ and $\mathbf{F}$ is the DTFT matrix. It should be noted that the last $(K-1)$ elements of $\hat{\mathbf{h}}_{1,i,p}$ and $\hat{\mathbf{h}}_{2,i,p}$ should be forced to be zero which can be seen as a noise removal step. The impulse response estimation described above should be performed for all azimuth bins and all elevation channels.

The estimated impulse responses for all elevation channels ($\forall i = 0, 1, ..., N_{\text{el}} - 1$) at a given range and azimuth bin can be expressed as the following,

$$\begin{aligned}\mathbf{h}_1[l, n_a] &= [h_{1,0}[l, n_a], h_{1,1}[l, n_a], ..., h_{1,(N_{\text{el}}-1)}[l, n_a]]^T \\ &= \underbrace{[\mathbf{a}(\phi_l) \quad \mathbf{a}(\phi_{l-l_d})]}_{\mathbf{A}_1(\phi_l)} \begin{bmatrix} h_{11}[l, n_a] \\ h_{21,d}[l, n_a] \end{bmatrix} \end{aligned} \tag{19}$$

$$\begin{aligned}\mathbf{h}_2[l, n_a] &= [h_{2,0}[l, n_a], h_{2,1}[l, n_a], ..., h_{2,(N_{\text{el}}-1)}[l, n_a]]^T \\ &= \underbrace{[\mathbf{a}(\phi_{l-l_d}) \quad \mathbf{a}(\phi_l)]}_{\mathbf{A}_2(\phi_l)} \begin{bmatrix} h_{12,d}[l, n_a] \\ h_{22}[l, n_a] \end{bmatrix} \end{aligned} \tag{20}$$

where,

$$\mathbf{a}(\phi_l) = [a_0(\phi_l), a_1(\phi_l), ..., a_{N_{\text{el}}-1}(\phi_l)]^T \tag{21}$$

$h_{11}[l, n_a]$ and $h_{21,d}[l, n_a]$ can be separated from $\mathbf{h}_1[l, n_a]$ and $h_{12,d}[l, n_a]$ and $h_{22}[l, n_a]$ can be separated from $\mathbf{h}_2[l, n_a]$ by multiplying $\mathbf{h}_1[l, n_a]$ and $\mathbf{h}_2[l, n_a]$ by the weight matrices $\mathbf{W}_1(\phi_l)$ $\mathbf{W}_2(\phi_l)$, respectively. The weight matrices can be obtained based on LCMV beamformer algorithm [7] as the following,

$$\mathbf{W}_1(\phi_l) = (\mathbf{A}_1^H(\phi_l)\mathbf{A}_1(\phi_l))^{-1}\mathbf{A}_1^H(\phi_l) \tag{22}$$

$$\mathbf{W}_2(\phi_l) = (\mathbf{A}_2^H(\phi_l)\mathbf{A}_2(\phi_l))^{-1}\mathbf{A}_2^H(\phi_l) \tag{23}$$

The impulse responses are separated for all azimuth and range bins. The delays in $h_{21,d}[l, n_a]$ and $h_{12,d}[l, n_a]$ can be easily compensated for in the range frequency domain by multiplying them with $e^{j2\pi f_r t_d}$to obtain $h_{21}[l, n_a]$ and $h_{12}[l, n_a]$ where f_r is the range frequency.

B. Azimuth Ambiguity Removal and Image Formation

As described previously, the impulse responses h_{11} and h_{21} occupies half the Doppler bandwidth ($B_d/N = B_d/2$) while h_{12} and h_{22} occupies the other half of the Doppler bandwidth. The Doppler spectra of impulse responses are aliased as the effective sampling frequency in the azimuth dimension is assumed to be ($\text{PRF} = B_d/(MN) = B_d/4$). The azimuth ambiguity removal of the half of the Doppler bandwidth will be now considered.

The Fourier transform of h_{11} and h_{21} across both azimuth and range dimensions can be expressed using the principle of displaced phase centre (DPC) [8] as the following,

$$H_{11}(f_r, f_a) = H_{21}(f_r, f_a)\underbrace{e^{j\pi d f_a/v_p}e^{j\pi d^2/(2\lambda R_l)}}_{Q_1(f_a)} \tag{24}$$

$$H_{21}(f_r, f_a) = H_{21}(f_r, f_a) \times \underbrace{1}_{Q_2(f_a)} \tag{25}$$

The aliased signals of $H_{11}(f_r, f_r)$ and $H_{21}(f_r, f_r)$ can be expressed as the following ($\forall m = 1, 2$),

$$\begin{aligned}\tilde{H}_{m1}(f_r, f_a) &= \sum_{k=-\infty}^{\infty} H_{m1}(f_r, f_a + kf_p) \\ &= \sum_{k=-\infty}^{\infty} H_{21}(f_r, f_a + kf_p)Q_m(f_a + kf_p)\end{aligned} \tag{26}$$

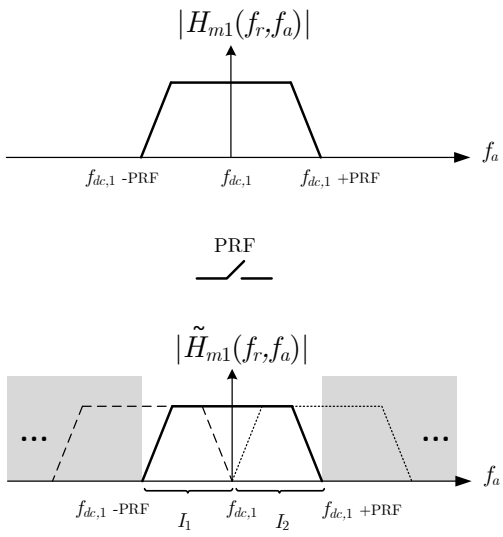

Fig. 3. The spectrum of the impulse response estimated at the first receiver when the transmitted signal is emitted by the m^{th} transmitter before and after sampling with PRF. $f_{dc,1}$ is Doppler centroid of the first receiver.

It is possible to weight and combine $\tilde{H}_{11}(f_r, f_a)$ and $\tilde{H}_{21}(f_r, f_a)$ in such a way that the original spectrum $H_{21}(f_r, f_a)$ is recovered while the back-folded component is removed as expressed in the following equations for the intervals I_1 and I_2 in Fig.3,

$$P_{11}(f_a)\tilde{H}_{11}(f_r, f_a) + P_{21}(f_a)\tilde{H}_{21}(f_r, f_a) = 2H_{21}(f_r, f_a) \tag{27}$$

$$P_{11}(f_a)\tilde{H}_{11}(f_r, f_a + f_p) + P_{21}(f_a)\tilde{H}_{21}(f_r, f_a + f_p) = 0 \tag{28}$$

For interval I_2 after shifting to I_1 to allow for setting up the linear systems of (31).

$$\begin{aligned}&P_{12}(f_a + f_p)\tilde{H}_{11}(f_r, f_a + f_p) + P_{22}(f_a + f_p)\tilde{H}_{21}(f_r, f_a + f_p) \\ &= 2H_{21}(f_r, f_a + f_p)\end{aligned} \tag{29}$$

$$P_{12}(f_a + f_p)\tilde{H}_{11}(f_r, f_a) + P_{22}(f_a + f_p)\tilde{H}_{21}(f_r, f_a) = 0 \tag{30}$$

The reconstruction filters can be computed as the following,

$$\mathbf{P}(f_a) = 2\mathbf{Q}^{-1}(f_a) \tag{31}$$

where,

$$\mathbf{Q}(f_a) = \begin{bmatrix} Q_1(f_a) & Q_2(f_a) \\ Q_1(f_a + \text{PRF}) & Q_2(f_a + \text{PRF}) \end{bmatrix}, \tag{32}$$

$$\mathbf{P}(f_a) = \begin{bmatrix} P_{11}(f_a) & P_{12}(f_a + \text{PRF}) \\ P_{21}(f_a) & P_{22}(f_a + \text{PRF}) \end{bmatrix} \tag{33}$$

I_2 is then concatenated with I_1 to obtain the original spectrum $H_{21}(f_r, f_a)$. Similarly, the original spectrum $H_{12}(f_r, f_a)$ is reconstructed using the aliased spectra of $H_{12}(f_r, f_a)$ and $H_{22}(f_r, f_a)$.

The impulse responses $H_{rx,1}(f_r, f_a) = H_{21}(f_r, f_a)$ and $H_{rx,2}(f_r, f_a) = H_{12}(f_r, f_a)$ have the same phase centre but each occupies half the Doppler bandwidth. The Doppler

centroids of $H_{rx,1}(f_r, f_a)$ and $H_{rx,2}(f_r, f_a)$ are functions of the squint angles θ_1 and θ_2. Without loss of generality, Range-Doppler algorithm is used for image formation [9]. The range cell migration correction (RCMC) is performed by multiplying $H_{rx,n}(f_r, f_a)$ by the following ($\forall n = 1, 2$),

$$H_{\mathrm{RCMC},n}(f_r, f_a) = e^{-j2\pi\Delta t_n(r_{\mathrm{ref}}, f_{a,n})f_r} \tag{34}$$

where,

$$\Delta t_n(r_{\mathrm{ref}}, f_{a,n}) = \frac{2}{c} r_{\mathrm{ref}}\big(1 - \frac{1}{\sqrt{1 - (\frac{\lambda f_{a,n}}{2v_p})^2}}\big), \tag{35}$$

$$\frac{-M\mathrm{PRF}}{2} + f_{dc,n} \leq f_{a,n} \leq \frac{M\mathrm{PRF}}{2} + f_{dc,n}, \tag{36}$$

r_{ref} is a reference range and $f_{dc,n}$ denotes the Doppler centroid of the n^{th} receiver. The full Doppler bandwidth is then synthesised before forming the image by performing the following steps [6]:

1) The data of each receiving beam after RCMC is converted into range time-Doppler domain.
2) The data of each receiving beam is then zero-padded in the Doppler dimension so that the points of each Doppler spectrum are increased by a factor of N.
3) Each zero-padded data is then frequency shifted in the Doppler dimension by the corresponding Doppler centroid to compensate for the Doppler shift introduced by the squint angle.
4) The data of all receiving beams are then added together to form the full Doppler bandwidth spectrum.

The resulted full Doppler bandwidth data in the range time-Doppler domain is multiplied by H_{RD} defined below to perform azimuth compression.

$$H_{\mathrm{RD}}(n_t, f_d; r_{\mathrm{ref}}) = \exp\left[\frac{j2\pi r_{\mathrm{ref}}}{v_p}\sqrt{f_{am}^2 - f_d^2}\right] \tag{37}$$

$$\frac{-NM\mathrm{PRF}}{2} \leq f_d \leq \frac{NM\mathrm{PRF}}{2} \tag{38}$$

where $f_{am} = 2v_p/\lambda$. The inverse azimuth Fourier transform is finally taken to obtain the image.

IV. Simulation Results

The following section shows the numerical results of our proposed MIMO SAR configuration using an LFM waveform and compares with a conventional MIMO SAR.

A. One Dimensional Echo Separation

Consider a scenario in which there are $M = 2$ transmit antennas, $N = 2$ receive antennas as shown in Fig.1, the number of elevation channels is $N_{\mathrm{el}} = 20$ and the channel impulse response length is $L = 1068$. The transmitted waveform is an LFM waveform with a bandwidth of $100MHz$ and the sampling frequency is $F_s = 200MHz$. The SNR in the simulation is assumed to be 40dB and the timing diagram of the transmission is as shown in Fig.2. Assume that there are two scatterers whose delays difference is $t_d = 1.333\mu s$ which is the same as the pulse width. This scenario (i.e. in which only the range dimension is considered) is presented to demonstrate how the received signals that correspond to different phase centres are separated at the receiver using digital beamforming (DBF) in elevation.

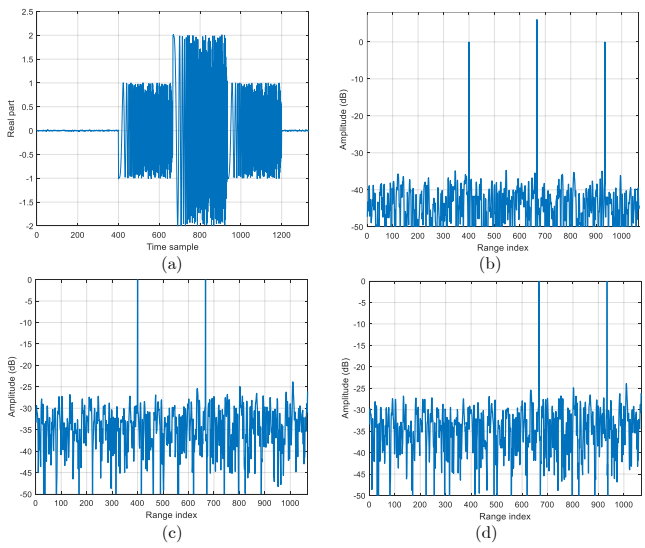

Fig. 4. One dimensional echo separation. (a) The real part of the received signal. (b) The estimated impulse response before the separation. (c) The separated impulse response whose phase centre is located at the centre of Tx1/Rx1. (d) The separated impulse response whose phase centre is located midway between Tx1/Rx1 and Tx2/Rx2 without delay compensation.

The received signal before the identification of the impulse response at the first receiver is as shown in Fig.4(a) and the estimated impulse response is as shown in Fig.4(b) where one can see that the impulse responses corresponding to different phase centres are overlapped. The separation is possible because echoes corresponding to different sub-pulses (at each instant of time) arrive from different elevation angles. The separated impulse response whose phase centre is located at the centre of Tx1/Rx1 is as shown in Fig.4(c) and the separated impulse response whose phase centre is located midway between Tx1/Rx1 and Tx2/Rx2 without delay compensation is as shown in Fig.4(d).

B. Azimuth Ambiguity Removal

Consider the simulation parameters listed in Table.I and assume that there two adjacent scatterers located at the swath centre. The azimuth and range cuts for the noiseless case are as shown in Fig.5 and Fig.6, respectively. It is clear from Fig.5 that there is no azimuth aliasing using our proposed MIMO configuration even though the PRF used is $B_d/(MN) = B_d/4 = 50Hz$ unlike the case of the conventional MIMO SAR in which minimum PRF should satisfy the inequality $\mathrm{PRF}_{min} \geq (B_d/K_p = B_d/3)$ where K_p is the number of non-overlapping phase centre which is equal to $(M + N - 1)$ when $M = N$. Accordingly, our proposed MIMO configuration outperforms the conventional MIMO SAR. It should be noted it has been assumed that the waveforms used in the conventional MIMO SAR are perfectly orthogonal. It should

TABLE I
SIMULATION PARAMETERS

Parameter	Symbol	Value
Number of Tx (Rx)	M (N)	2
Min. distance to the swath centre	R_0	$20km$
Look angle	ϕ	45^o
Azimuth length of the conventional MIMO SAR beamformer	L_a	$2m$
Azimuth length of the proposed MIMO SAR beamformer	$L_{a,\text{prop}}$	$4m$
Distance between adjacent Tx/Rx in (proposed) MIMO SAR	(d_{prop}) d	$(4m)$ $2m$
Doppler bandwidth	B_d	$200Hz$
Pulse repetition frequency	PRF	$50Hz$
Platform Velocity	v_p	$200m/s$
Carrier Frequency	F_c	$4.5GHz$
Sampling Frequency	F_s	$200MS/s$
Single waveform Bandwidth	BW	$100MHz$
Number of elevation channels	N_{el}	10
Pulse width	τ	$2.5\mu s$

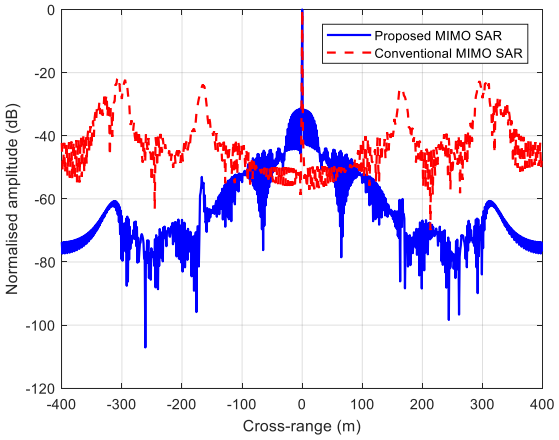

Fig. 5. The azimuth cut of a scatterer in the estimated scene using the proposed and conventional MIMO SAR.

be pointed out that the effect of the inter-beams overlapping on the azimuth ambiguity due to the side-lobes of the narrow azimuth beams is not considered here but it will be studied and mitigated in future work.

V. CONCLUSION

In this paper, a new MIMO SAR configuration with multiple adjacent azimuth beams is proposed to obtain high resolution wide swath imaging. The proposed configuration utilises all the phase centres including the overlapping ones which allows to use a lower operating PRF as compared with the conventional MIMO SAR. The waveforms used for transmission consists of a sequence of LFM waveforms which share the same bandwidth and have the same centre frequency. Echoes corresponding to different phase centres are separated at the receiver using DBF on receive in elevation. The use of such waveforms simplify the implementations and hence gains all of

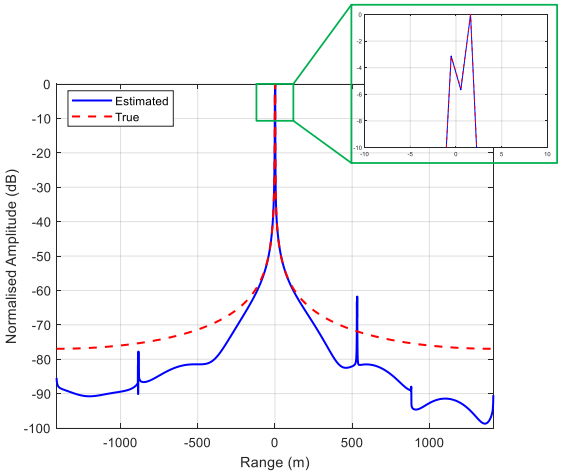

Fig. 6. The range cut of the true and estimated scene.

LFM inherent benefits (e.g. constant envelop and unity peak to average power). Finally, the simulation results validate that the proposed configuration outperforms the conventional MIMO SAR.

ACKNOWLEDGMENT

The first author would like to acknowledge the support of King Abdulaziz City for Science and Technology (KACST) in Saudi Arabia.

REFERENCES

[1] G. Krieger, N. Gebert, and A. Moreira, "High-resolution synthetic aperture side view radar system used by means of digital beamforming," 2007.
[2] G. Krieger, "MIMO-SAR: Opportunities and pitfalls," *IEEE Transactions on Geoscience and Remote Sensing*, vol. 52, no. 5, pp. 2628–2645, 2014.
[3] W. Q. Wang, "Mitigating range ambiguities in high-PRF SAR with OFDM waveform diversity," *IEEE Geoscience and Remote Sensing Letters*, vol. 10, no. 1, pp. 101–105, 2013.
[4] W. Q. Wang and J. Cai, "Ground moving target indication by MIMO SAR with multi-antenna in azimuth," in *International Geoscience and Remote Sensing Symposium (IGARSS)*, 2011, pp. 1662–1665.
[5] W. Wang, R. Wang, Y. Deng, L. Hou, W. Xu, and L. Guo, "A processing scheme for LFM-based waveform MIMO SAR with digital beam-forming in elevation," *Remote Sensing Letters*, vol. 6, no. 11, pp. 874–883, 2015. [Online]. Available: https://doi.org/10.1080/2150704X.2015.1088672
[6] M. AlShaya, M. Yaghoobi, and B. Mulgrew, "Multiple-Beam IRCI-Free MIMO SAR," in *2019 International Radar Conference (Radar)*, Toulon, 2019.
[7] Harry L. Van Trees, *Optimum Array Processing: Part IV of Detection, Estimation, and Modulation Theory*, 2002.
[8] M. AlShaya, M. Yaghoobi, and B. Mulgrew, "Frequency Domain System Identification for Wide Swath High Resolution IRCI-Free MIMO SAR," in *2019 IEEE Radar Conference (RadarConf19)*, Boston, 2019.
[9] R. Bamler, "A Comparison of Range-Doppler and Wavenumber Domain SAR Focusing Algorithms," *IEEE Transactions on Geoscience and Remote Sensing*, 1992.